Quantum transport at the Dirac point: Mapping out the minimum conductivity from pristine to disordered graphene

Redwan N. Sajjad*
Department of Electrical Engineering and Computer Science, Massachusetts Institute of Technology, Cambridge, Massachusetts 02139, USA

Frank Tseng
Naval Research Laboratory, Washington D.C. 20375, USA

K. M. Masum Habib and Avik W. Ghosh
Department of Electrical and Computer Engineering, University of Virginia, Virginia 22904, USA
(Received 2 July 2015; revised manuscript received 8 September 2015; published 5 November 2015)

The phase space for graphene's minimum conductivity $\sigma_{\min}$ is mapped out using Landauer theory modified for scattering using Fermi's golden rule, as well as the nonequilibrium Green's function (NEGF) simulation with a random distribution of impurity centers. The resulting "fan diagram" spans the range from ballistic to diffusive over varying aspect ratios (W/L), and bears several surprises. The device aspect ratio determines how much tunneling (between contacts) is allowed and becomes the dominant factor for the evolution of $\sigma_{\min}$ from ballistic to diffusive regime. We find an increasing (for $W/L > 1$) or decreasing ($W/L < 1$) trend in $\sigma_{\min}$ vs impurity density, all converging around $128q^2/\pi^3 h \sim 4q^2/h$ at the dirty limit. In the diffusive limit, the conductivity quasisaturates due to the precise cancellation between the increase in conducting modes from charge puddles vs the reduction in average transmission from scattering at the Dirac point. In the clean ballistic limit, the calculated conductivity of the lowest mode shows a surprising absence of Fabry-Pérot oscillations, unlike other materials including bilayer graphene. We argue that the lack of oscillations even at low temperature is a signature of Klein tunneling.

DOI: 10.1103/PhysRevB.92.205408 PACS number(s): 72.80.Vp, 73.63.−b, 72.10.−d

I. INTRODUCTION

Since its discovery in the last decade, single layer graphene has catalyzed widespread research [1] stemming from its extraordinary material properties. Multiple electronic, spintronic, and optoelectronic applications are predicted to arise from the entire class of 2D materials emergent in graphene's footsteps [2]. Despite intense scrutiny, there exist many unresolved issues that continue to make the material fascinating. Among them is the physics of the minimum conductivity, $\sigma_{\min}$ around the Dirac point, where the density of states is expected to vanish. Instead of vanishing accordingly, $\sigma_{\min}$ for a ballistic sheet with large width to length aspect ratio ($W/L \gg 1$) is shown to be a universal constant $\sigma_Q = 4q^2/(\pi h)$ [3,4]. This arises from the preponderance of tunneling through a continuum of subbands with near zero band gaps. In these structures ($W \gg L$ samples), a series of exponentially decaying tunnel transmissions adds up to an overall Ohmic term that factors out of the ballistic conductance $G = \sigma W/L$. Measured $\sigma_{\min}$s, however, are typically in the range 4–$12q^2/h$ [5,7–9], except Ref. [3], larger than σ_Q. This is surprising given that these experiments are mostly on dirty samples where we expect the conductivity to be not only nonuniversal but certainly smaller than the ballistic limit. The increase in $\sigma_{\min}$ from σ_Q arises from charged impurities on the substrates that create electron and hole puddles and contribute states to the charge neutrality point [10]. However an opposite, decreasing trend of $\sigma_{\min}$ vs impurity concentration (n_{imp}) was demonstrated theoretically by Adam *et al.* in Ref. [6] within Boltzmann transport theory, as well as experimentally in Ref. [5]. Clearly there are several disjointed pieces that have yet to come together to provide a complete phase picture of the evolution of $\sigma_{\min}$ with sample quality.

In this paper, we use quasianalytical Landauer equation as well as numerical NEGF (within the Fisher-Lee formulation) [11] to map out the entire phase space of $\sigma_{\min}$ for varying n_{imp} and W/L (Fig. 1). Our results clearly show that the missing link is the total tunneling current (a function of W/L), a piece of physics typically ignored in semiclassical models. The observed quasisaturation arises due to a tradeoff between the number of modes and the scattering time τ from charge puddles, as we move from the ballistic to diffusive regime. The total conductivity can be written as

$$\sigma = G_0[M_p T_p + M_e T_e]L/W, \tag{1}$$

where $G_0 = 4q^2/h$ is conductance quantum including spin and valley degeneracy, M_p and M_e are the number of propagating and evanescent modes, and T is the corresponding mode averaged transmission probability. While this equation defines an absolute lower bound on conductivity at $\sigma_Q = 4q^2/(\pi h)$ (dashed line in Fig. 1 top), we will shortly show that for dirty samples with impurity density $\sim 3 - 5 \times 10^{12}/\text{cm}^2$, it predicts a quasisaturating $\sigma_{\min} \approx 4q^2/h$, consistent with experiments (Fig. 1). Part of the fan diagram for $W \ll L$, the decreasing trend in $\sigma_{\min}$ in Fig. 1 obtained earlier using the Boltzmann transport equation, arises naturally in our model from scattering of the propagating modes $\sigma \propto G_0[M_p T_p]$, where $M_p T_p \propto \sqrt{n_0^2 + n_{\text{imp}}^2}/n_{\text{imp}} = \sqrt{1 + n_0^2/n_{\text{imp}}^2}$ (n_0 is the background doping). For the opposite ballistic limit, wide samples have a conductivity that dips down to the quantized value σ_Q to generate the rest of the fan diagram. At the same time, narrow ballistic samples with limited tunneling show a *conductance* quantization G_0 that bears a spectacular

*redwansajjad@gmail.com

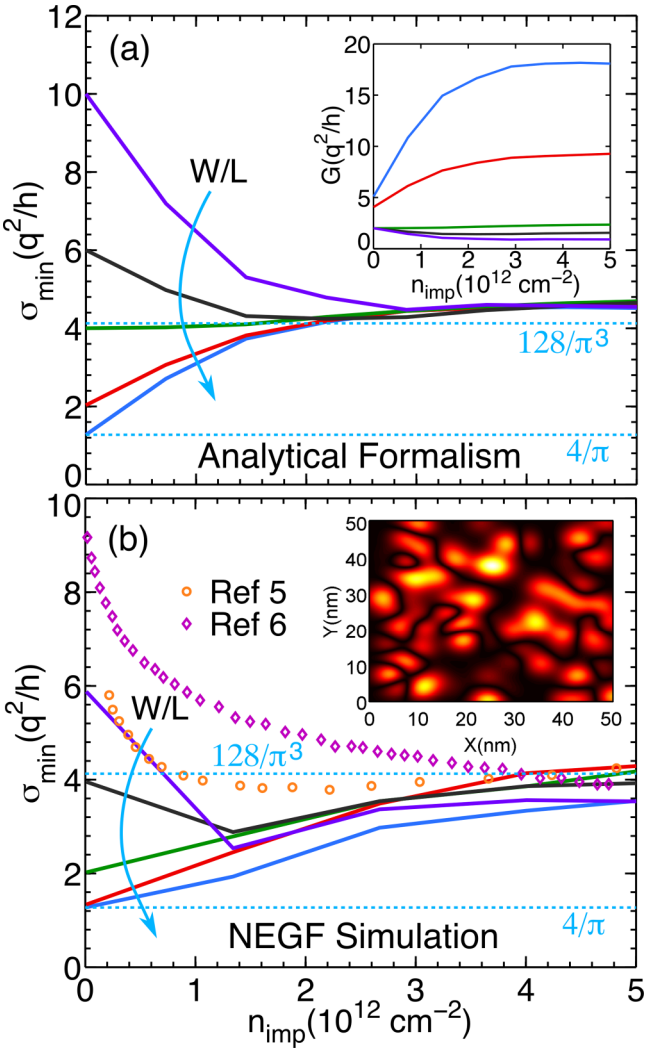

FIG. 1. (Color online) (a) Fan diagram of quasianalytical $\sigma_{\min}$ for $W = 500$ nm with varying W/L (inset shows conductance G), $L =$ 125 nm, 250 nm, 1 μm, 1.5 μm, 2.5 μm. The ballistic $\sigma_{\min}$ is exactly at $\sigma_Q = 4q^2/\pi h$. The two new features are (1) quasisaturation at high impurity density to $\sim 128q^2/\pi^3 h$ and (2) a flip in curvature between aspect ratios. (b) NEGF calculated $\sigma_{\min}$ averaged over puddle geometries (inset). The data saturate at $\sim 4q^2/h$ in dirty graphene. Orange circle is experimental data from Ref. [5] and purple diamond is theoretical prediction from Ref. [6].

robustness with temperature and a remarkable absence of Fabry Pérot (FP) resonance even at low temperature. We interpret the absence of FP (Fig. 3) as a clear signature of Klein tunneling, where the linear relativistic electron transmits perfectly at normal incidence due to pseudospin conservation, contrary to the prediction of nonrelativistic Schrödinger equation (which applies to bilayer graphene as we show). Our results are supported by numerical NEGF sampled over a random distribution of charged impurities.

II. MODELING CHARGED IMPURITIES

The lack of dangling bonds makes direct chemisorption of charged impurities difficult on graphene. However, dielectric substrates can have charged impurities that play a

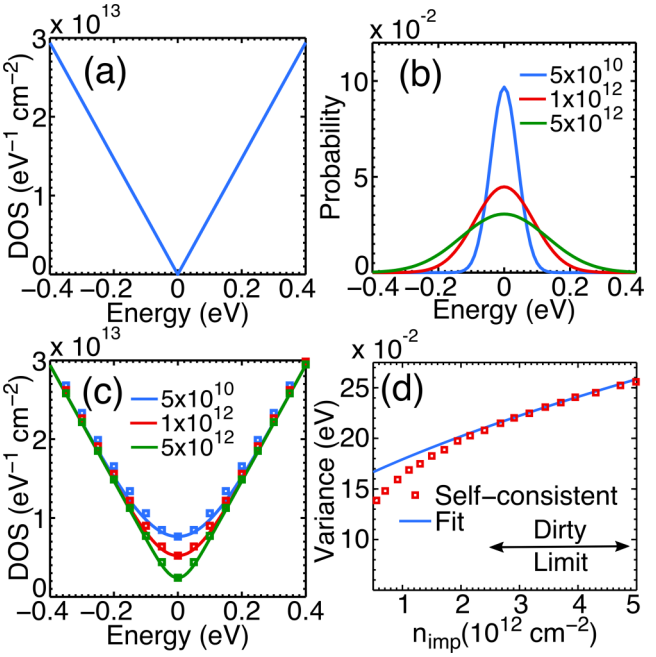

FIG. 2. (Color online) Averaging (a) the pristine graphene density of states with (b) a normal distribution of random potentials (c) erases the Dirac point. (d) The variance of the Gaussian is calculated self-consistently and refitted with a simplified expression Eq. (9), closely matching with the self-consistent calculation in the dirty limit.

significant role on transport around graphene's Dirac point. The physisorption of charged impurities randomly dopes the graphene, creating a Gaussian distribution in the energy of Dirac points around neutrality. The resulting erasure of the Dirac point is seen in quantum capacitance measurements [12]. We can average the linear density of states of graphene (D) [Fig. 2(a)] over a Gaussian distribution of potentials [Fig. 2(b)], with zero average potential E_0, variance σ_E. Assuming a Gaussian distribution of dopants that in turn create a Gaussian distribution of shifts E_c around the Dirac point with an average shift E_0, we get the modified density of states (D_{puddle})

$$D_{\text{puddle}} = \sum_{E_c} D(E - E_c)P(E_c) \tag{2}$$

$$P(E_c) = \frac{1}{\sigma_E\sqrt{2\pi}} e^{-(E_c - E_0)^2/2\sigma_E^2}. \tag{3}$$

Note that we are assuming that the puddles have no "memory," i.e., a Gaussian white noise, so that the correlation between two different energy fluctuations at E_c and E_c' acts like a delta function $C(E_c, E_c') = \sigma_E^2\delta(E_c - E_c')$. Integrating the linear density of states over the Gaussian distribution of shifted Dirac points, we get

$$D_{\text{puddle}}(E) = \frac{2\sqrt{\frac{2}{\pi}}\sigma_E e^{-E^2/2\sigma_E^2} + 2|E|\text{erf}\left(\frac{|E|}{\sigma_E\sqrt{2}}\right)}{\pi\hbar^2 v_F^2}. \tag{4}$$

This expression of the density of states involving error functions was also worked out by Li *et al.* [13], but we can express it in a simpler form that interpolates between the

low-energy parabolic and high-energy linear behavior:

$$D_{\text{puddle}}(E) \approx \frac{2\sqrt{E^2 + 2\sigma_E^2/\pi}}{\pi \hbar^2 v_F^2}. \quad (5)$$

In Fig. 2(c), we see that such approximation matches the exact expression very well. This also allows us to have a compact expression of the minimum conductivity as we show later. Equation (5) shows that the variance σ_E has a direct impact on the minimum density of states. Figure 2(d) shows that σ_E increases with charged impurity concentration, so that *the minimum number of modes for conduction is proportional to the statistical variance of charge impurities.* This has also been worked out by solving Poisson's equation in cylindrical coordinates [13]

$$\sigma_E^2 = 2\pi n_{\text{imp}} q^2 \int [A_k]^2 k\, dk \quad (6)$$

$$A_k = \frac{2e^{-\kappa z_0} Zq \sinh(k\, d)}{k\kappa_{ins}\cosh(k\, d) + (k\kappa_v + 2\, q_{TF}\kappa)\sinh(k\, d)} \quad (7)$$

$$q_{TF} = 2\pi q^2/\kappa D_{\text{puddle}}(E). \quad (8)$$

κ_v and κ_{ins} are the respective vacuum and insulator dielectric constants, while κ is their average. Equation (8) defines the Thomas-Fermi screening wave vector which depends on the average density of states [Eq. (4)]. A_k is the potential solved from Poisson's equation which accounts for the distance of the impurities (z_o) inside the oxide, thickness of the oxide (d), and the screening length ($1/q_{TF}$). Solved self-consistently between σ_E and D_{puddle} [Eqs. (5)–(8)], we determine the variance of the normal distribution of potentials [Fig. 2(d)]. Over the dirty range, we can simplify it with a fitted equation

$$\sigma_E^2 \approx 2\hbar^2 v_F^2 n_{\text{imp}} + C \quad (9)$$

where $C = 0.027\,\text{eV}^2$. This equation closely approximates the self-consistent calculation especially at the dirty limit. The variation of $\sigma_{\min}$ in the presence of charged impurities allows us to quantify the competition between increasing modes and increased scattering.

III. ANALYTICAL MODEL FOR $\sigma_{\min}$

The Landauer conductivity intuitively frames conduction as proportional to the transmission probability of electrons T_n summed over all propagating and evanescent modes, where n is the mode index:

$$\sigma_{\min} = G\, L/W = \frac{4q^2}{h} \sum_{n=0}^{\infty} T_n \frac{L}{W}. \quad (10)$$

The general form for T_n, derivable by matching the pseudospinor wave functions across an n-p-n or p-n-p junction with barrier height U_0 gives [4]

$$T_n = \left| \frac{k_n}{k_n \cos k_n L + i(U_o/\hbar v_F)\sin k_n L} \right|^2, \quad (11)$$

where $k_n = \sqrt{(U_o/\hbar v_F)^2 - q_n^2}$ and $q_n = n\pi/W$ (for "metallic armchair" edge) is the transverse wave vector in the channel that we sum over to get the total transmission. When k_n is real then the transverse modes are propagating, while when k_n is imaginary they become evanescent. Imaginary k_n changes all the trigonometric functions to hyperbolic functions giving us an evanescent transmission $T_e = 1/\cosh^2 q_n L$ when U_o is zero. An integral over a continuum of such cosh contributions gives an overall factor of $W/\pi L$ which leads to the ballistic conductivity quantization (σ_Q). For propagating modes, the transmission probability T_p picks up an additional scattering coefficient term from a series sum over the multiple scattering history, $\lambda/(\lambda + L)$, where λ is the electron mean free path in the presence of embedded impurities. The mean free path is $v_F \tau_{sc}$ where the momentum scattering time τ_{sc} is determined from Fermi's golden rule below. Combining all the elements in Eq. (1), we arrive at the fan diagram in Fig. 1.

Impurity scattering occurs through a 2D screened Coulomb energy, given at long wavelength by the Thomas Fermi equation,

$$V_C(\mathbf{r}) = \frac{q^2}{4\pi\epsilon_0 r} e^{-\kappa r}. \quad (12)$$

Using the pseudospin eigenstates, $\Psi_{i,f}(\mathbf{r}) = 1/\sqrt{2S}\,(1\;\; e^{i\theta_{i,f}})^T e^{i\mathbf{k}_i \cdot r}$ normalized over area S, we calculate the scattering matrix element $V_{if} = \int d^2\mathbf{r}\Psi_f^*(\mathbf{r})V_C(\mathbf{r})\Psi_i(\mathbf{r})$. In terms of scattering wave vector and angle $\Delta\mathbf{k} = \mathbf{k_f} - \mathbf{k_i}$, $\Delta\theta = \theta_f - \theta_i$,

$$\begin{aligned}
V_{if} &= \frac{1}{2S}\int d^2\vec{r} e^{i\Delta\vec{k}\cdot\vec{r}}[1 + e^{i\Delta\theta}]\frac{q^2}{4\pi\epsilon_0 r}e^{-\kappa r}, \\
V_{if} &= \frac{1}{2S}[1 + e^{i\Delta\theta}]\int_0^\infty r dr \frac{q^2 e^{-\kappa r}}{4\pi\epsilon_0 r}\int_0^{2\pi} d\theta e^{i\Delta k r\cos\theta}, \\
V_{if} &= \frac{q^2}{4\epsilon_0 S}[1 + e^{i\Delta\theta}]\int_0^\infty dr J_0(\Delta k r)e^{-\kappa r}, \\
V_{if} &= \frac{q^2}{4\epsilon_0 S\sqrt{\Delta k^2 + \kappa^2}}[1 + e^{i\Delta\theta}].
\end{aligned} \quad (13)$$

We have used the Bessel function of the first kind (of order zero), J_0, and its Laplace transform. We can change to energy variables for elastic scattering using $|\mathbf{k}_f| = |\mathbf{k}_i| = E/(\hbar v_F)$, $(\Delta k)^2 = |\mathbf{k}_f - \mathbf{k}_i|^2 = k_f^2 + k_i^2 - 2k_f k_i \cos\Delta\theta = 2E^2(1 - \cos\Delta\theta)/(\hbar^2 v_F^2)$. We get

$$|V_{if}|^2 = \frac{q^4\hbar^2 v_F^2(1 + \cos\Delta\theta)}{8\epsilon_0^2 S^2\left[2E^2(1 - \cos\Delta\theta) + \hbar^2 v_F^2\kappa^2\right]}. \quad (14)$$

For an impurity density n_{imp} and cross-sectional area S (i.e., number of impurities $n_{\text{imp}}S$), Fermi's golden rule now gives us

$$\hbar/\tau_{sc} = \sum_{\mathbf{f}} |V_{if}|^2 \delta(E - E_k)(1 - \cos\theta_k) n_{\text{imp}} S. \quad (15)$$

Converting sum into integral using the density of states [Eq. (5)] and using the calculated expression for $|V_{if}|^2$ simplified for low energies, we get

$$\begin{aligned}
\frac{\hbar}{\tau_{sc}} = \frac{q^4\hbar^2 v_F^2 n_{\text{imp}}}{16\epsilon_0^2\pi} &\int D_{\text{puddle}}(E_k) dE_k \delta(E - E_k) \\
&\times \int d\Delta\theta \frac{1 - \cos^2\Delta\theta}{2E_k^2(1 - \cos\Delta\theta) + \hbar^2 v_F^2\kappa^2}.
\end{aligned} \quad (16)$$

The cosine integral followed by the delta function energy integral gives us

$$\frac{\hbar}{\tau_{sc}} = \frac{q^4\hbar^2 v_F^2 n_{\rm imp}}{16\epsilon_0^2\pi} D_{\rm puddle}(E)\frac{\pi}{2E^4} \times \left[2E^2 + \hbar^2 v_F^2\kappa^2 - \hbar v_F\kappa\sqrt{4E^2 + \hbar^2 v_F^2\kappa^2}\right] \quad (17)$$

with $D_{\rm puddle}$ defined in Eq. (5). For $E \ll \hbar v_F\kappa$, the term in square brackets expands to $2E^4/\hbar^2 v_F^2\kappa^2 + O(E^6/\hbar^4 v_F^4\kappa^4)$. We then get

$$\frac{\hbar}{\tau_{sc}} \approx \frac{q^4 n_{\rm imp} D_{\rm puddle}}{16\epsilon_0^2\kappa^2} \quad (18)$$

with $\kappa = q^2 D_{\rm puddle}/\epsilon_0$, giving us $\hbar/\tau_{sc} = (n_{\rm imp}/16)D_{\rm puddle}$. Using the Einstein relation (diffusion coefficient $\mathcal{D} = v_F^2\tau_{sc}/2$), we get

$$\sigma_{\rm min} = q^2 D_{\rm puddle}\mathcal{D} = \frac{8q^2 v_F^2\hbar}{n_{\rm imp}} D_{\rm puddle}^2. \quad (19)$$

At high impurity density, $D_{\rm puddle}^2 \approx 8\sigma_E^2/\pi^3\hbar^4 v_F^4$ [Eq. (5)]. Using the approximate relation from Eq. (9) matching the self-consistent calculation fairly well in the dirty limit (Fig. 2), we get

$$\lim_{n_{\rm imp}\to\infty}\sigma_{\rm min} \approx \frac{128q^2}{\pi^3 h} = 4.12\frac{q^2}{h}. \quad (20)$$

IV. NUMERICAL MODEL FOR $\sigma_{\rm min}$

We now show NEGF based numerical simulation results to calculate $\sigma_{\rm min}$ in the presence of charged impurities. First we briefly introduce the main equations used in our numerical calculations for NEGF. The central quantity is the retarded Green's function,

$$\mathcal{G}(E) = (E\mathcal{I} - H - U - \Sigma_1 - \Sigma_2)^{-1}. \quad (21)$$

H is found from a discretized version of the $k\cdot p$ Hamiltonian, U is the electrostatic potential in the device, and $\Sigma_{1,2}$ are the self energy matrices for the semi-infinite source and drain leads calculated from surface Green's function g_s. We recursively calculate g_s for doped graphene contacts, the doping related to the contact work function. We assume that the Fermi level is pinned under the contact and thus energy independent. Assuming an effective doping ΔE_F under the contacts. The effective contact surface Green's function is calculated from

$$g_s = (\Delta E_F\mathcal{I} - H - \tau^\dagger g_s\tau)^{-1} \quad (22)$$

which is solved iteratively using a decimation technique [14] using $\Delta E_F = 0.25$ eV. Then $\Sigma = \tau^\dagger g_s\tau$, where τ is the unit cell to unit cell coupling matrix. The total conductance is calculated,

$$G = Tr(\Gamma_1\mathcal{G}\Gamma_2\mathcal{G}^\dagger) \quad (23)$$

in units of q^2/h; $\Gamma_{1,2}$ are the anti-Hermitian parts of self energy representing the energy level broadening associated with charge injection and removal in and out of the contacts. To expedite computation, we employ recursive Green's function algorithm (RGFA) [15] to perform Eqs. (21)–(23).

We use a discretized $k\cdot p$ Hamiltonian (H) to reduce matrix size and expedite computation. The Hamiltonian for graphene at low energy is modified as

$$H(k) = \hbar v_F\left[k_x\sigma_x + k_y\sigma_y + \beta\left(k_x^2 + k_y^2\right)\sigma_z\right], \quad (24)$$

where v_F is the Fermi velocity, $\vec{k} = k_x\hat{x} + k_y\hat{y}$ is the wave vector, σ's are Pauli matrices, and $\hbar$ is the reduced Plank's constant. The extra term $\beta(k_x^2 + k_y^2)\sigma_z$ allows us to generate a computationally efficient Hamiltonian using a course grid without sacrificing accuracy. The k-space Hamiltonian in Eq. (24) is transformed to a real-space Hamiltonian by replacing k_x with differential operator $-i\frac{\partial}{\partial x}$, k_x^2 with $-\frac{\partial^2}{\partial x^2}$ etc. The differential operators are then discretized using the finite difference method for the NEGF calculation. We use grid spacing $a = 20$ Å and $\beta = 23$ Å, for which the band structure is accurate up to sufficiently large energy level ($\sim\pm 0.75$ eV). A more detailed description of the $k\cdot p$ method used can be found in Ref. [16].

We then use a sequence of Gaussian potential profiles for the impurity scattering centers,

$$U(r) = \sum_{n=1}^{n_{\rm imp}} U_n \exp\left(-|r - r_n|^2/2\zeta^2\right), \quad (25)$$

specifying the strength of the impurity potential at atomic site r, with r_n being the positions of the impurity atoms and ζ the screening length ($\sim$3 nm). The amplitudes U_n are random numbers following a Gaussian distribution with a standard deviation of 100 meV [8]. This standard deviation is to be differentiated from the standard deviation in the density of states description [Eq. (5)], which is a lumped description for the entire sheet instead of individual impurities. The Gaussian profile [Eq. (25)] is used to prevent the potential from going to infinity at the scattering centers (Thomas-Fermi), and such an approach is widely employed in the literature [8,17–20]. With U added to H, we calculate $\sigma_{\rm min}$ as a function $n_{\rm imp}$ [Fig. 1(b)] by calculating average conductance over $\sim$800 random impurity configurations. We keep the width fixed at $W = 500$ nm and perform the simulation for $L = 125$ nm, 250 nm, 1 μm, 1.5 μm, and 2.5 μm. In the ballistic limit, $\sigma_{\rm min}$ varies linearly with L/W, but as the sample gets dirtier, the $\sigma_{\rm min}$ becomes less dependent on L/W. At high impurity limit, $\sigma_{\rm min}$ becomes weakly dependent on $n_{\rm imp}$ and saturates around $4q^2/h$. In most experiments, the device length L is larger than width W, and therefore we see a decreasing trend for $\sigma_{\rm min}$ vs $n_{\rm imp}$ such as in Ref. [5]. The evolution of $\sigma_{\rm min}$ is from $4q^2/(\pi h)$ to $\sim 4q^2/h$, and therefore the missing π can only be seen for devices with $W \gg L$. The differences between the numerical and the analytical approaches most likely originate from the lack of adequate samples.

V. ABSENCE OF FABRY-PÉROT AS A SIGNATURE OF KLEIN TUNNELING

We now take a closer look at the conductance near the Dirac point at the ballistic limit with a motivation to demonstrate the difference between single layer and bilayer graphene. We employ the same numerical formalism [Eqs. (21)–(23)] but this time with a 1 p_z orbital basis tight binding Hamiltonian with a 40 nm × 40 nm wide graphene sheet (armchair edge). Due to

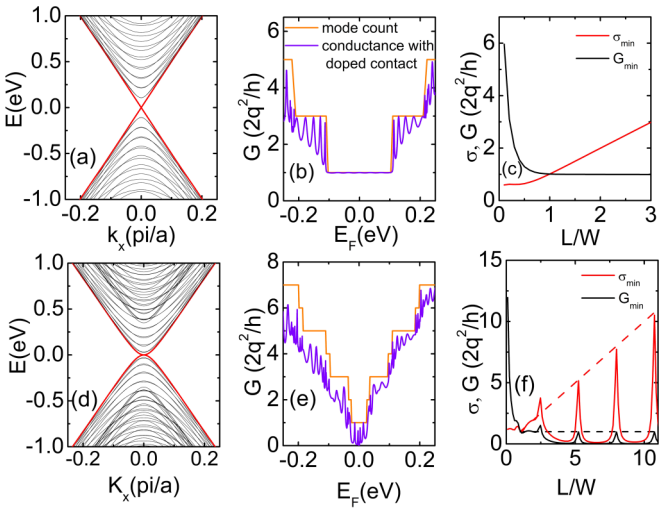

FIG. 3. (Color online) NEGF calculation of total conductance G of single layer graphene and bilayer graphene reveals the nature of Fabry-Pérot oscillation for the lowest mode. (a),(d) show linear and parabolic $E-K$ in single layer and bilayer graphene. The lowest mode in single layer does not show any oscillation (b) but the bilayer does (e). The variation of minimum conductance and conductivity for single layer shows saturating $G_{\min}$ at $2q^2/h$ (c), while for bilayer graphene the minimum conductance never saturates and produces oscillation in both $G_{\min}$ and $\sigma_{\min}$ (f).

nonuniform doping along the metal-graphene-metal captured in our model by the differential dopings, a Fabry-Pérot cavity is formed. Such a cavity leads to quantum interference oscillations and conductance asymmetry (n-n-n vs n-p-n doping), seen in Fig. 3 in the ballistic limit. Such oscillations have been seen experimentally at low temperature in 2DEGs [21] but are conspicuously missing for the lowest mode in single layer graphene (SLG), as seen in Fig. 3(b). In contrast, the higher modes show oscillations, as do all the modes for bilayer graphene (BLG) seen in Fig. 3(e). The lowest mode in single layer graphene has forward and reverse propagating $E-k$ bands with opposite pseudospin indices (bonding vs antibonding combinations of dimer p_z orbitals) that disallow any reflection at heterojunctions. The resulting Klein tunneling [22] makes the heterojunctions completely transparent to the lowest propagating modes and eliminates any Fabry-Pérot oscillations. The parabolic lowest bands of BLG have twice the winding number around the Fermi circle (angle $2\theta_{i,f}$ in the pseudospin eigenstate $\Psi_{i,f}$) and thus a common pseudospin index, leading to finite reflection and Fabry-Pérot oscillations.

We thus expect distinct behaviors of $\sigma_{\min}$ vs L/W in single layer and bilayer graphene. For large L/W, $G_{\min}$ for SLG approaches $2q^2/h$ eliminating all tunneling modes from source to drain and $\sigma_{\min}=GL/W$ increases linearly [Figs. 3(a)–3(c)], already demonstrated in experiment [3]. For BLG [Figs. 3(d)–3(f)], the conductance oscillation for the lowest mode is manifested in the length dependence as well, leading to an oscillation in both $G_{\min}$ and $\sigma_{\min}$. For small L/W, the $\sigma_{\min}$ saturates to $4q^2/(\pi h)$ and $2q^2/h$ for SLG and BLG, respectively [4,23]. Such nontrivial transport behavior near the Dirac point is a measurable signature of Klein tunnel and reflection.

VI. CONCLUSION

The composite phase plot of graphene's minimum conductivity is presented within a unified Landauer-Fermi's golden rule and NEGF transport model. We show a general convergence of $\sigma_{\min}$ vs impurity concentration along with a quasisaturation at high impurity concentration to $\sim 4q^2/h$ irrespective of device dimensions. For high aspect ratios the increase in density of states due to charged impurities results in a logarithmically increasing $\sigma_{\min}$ from the ballistic limit. On the other hand, for low aspect ratios the scattering due to charged impurities dominates and results in a power law decrease in the $\sigma_{\min}$. For clean samples with conductance quantization, gating the sample into its lowest mode reveals a striking absence of low-temperature Fabry-Pérot oscillations at low temperatures for SLG but not BLG, providing a signature of Klein tunneling.

ACKNOWLEDGMENTS

This work was financially supported by the NRI-INDEX center. The authors thank Eugene Kolomeisky (UVa) and Enrico Rossi (CWM) for useful discussions.

[1] A. K. Geim and K. S. Novoselov, Nat. Mater. **6**, 183 (2007).
[2] G. Fiori, F. Bonaccorso, G. Iannaccone, T. Palacios, D. Neumaier, A. Seabaugh, S. K. Banerjee, and L. Colombo, Nat. Nanotechnol. **9**, 768 (2014).
[3] F. Miao, S. Wijeratne, Y. Zhang, U. C. Coskun, W. Bao, and C. N. Lau, Science **317**, 1530 (2007).
[4] J. Tworzydło, B. Trauzettel, M. Titov, A. Rycerz, and C. W. J. Beenakker, Phys. Rev. Lett. **96**, 246802 (2006).
[5] J.-H. Chen, C. Jang, S. Adam, M. S. Fuhrer, E. D. Williams, and M. Ishigami, Nat. Phys **4**, 377 (2008).
[6] S. Adam, E. Hwang, V. Galitski, and S. Das Sarma, Proc. Natl. Acad. Sci. **104**, 18392 (2007).
[7] Y.-W. Tan, Y. Zhang, K. Bolotin, Y. Zhao, S. Adam, E. H. Hwang, S. Das Sarma, H. L. Stormer, and P. Kim, Phys. Rev. Lett. **99**, 246803 (2007).
[8] Y. Sui, T. Low, M. Lundstrom, and J. Appenzeller, Nano Lett. **11**, 1319 (2011).
[9] F. Amet, J. R. Williams, K. Watanabe, T. Taniguchi, and D. Goldhaber-Gordon, Phys. Rev. Lett. **110**, 216601 (2013).
[10] J. Martin, N. Akerman, G. Ulbricht, T. Lohmann, J. Smet, K. Von Klitzing, and A. Yacoby, Nat. Phys. **4**, 144 (2007).
[11] S. Datta, *Quantum transport: atom to transistor* (Cambridge University Press, New York, 2005).
[12] Y. Zhang, V. W. Brar, C. Girit, A. Zettl, and M. F. Crommie, Nat. Phys. **5**, 722 (2009).
[13] Q. Li, E. H. Hwang, and S. D. Sarma, Phys. Rev. B **84**, 115442 (2011).
[14] M. Galperin, S. Toledo, and A. Nitzan, J. Chem. Phys. **117**, 10817 (2002).
[15] K. Alam and R. K. Lake, J. Appl. Phys.. **98**, 064307 (2005).

[16] K. M. Habib, R. N. Sajjad, and A. W. Ghosh, arXiv:1509.01517.
[17] J. W. Kłos and I. V. Zozoulenko, Phys. Rev. B **82**, 081414 (2010).
[18] C. H. Lewenkopf, E. R. Mucciolo, and A. H. Castro Neto, Phys. Rev. B **77**, 081410 (2008).
[19] S. Adam, P. W. Brouwer, and S. Das Sarma, Phys. Rev. B **79**, 201404 (2009).
[20] A. Rycerz, J. Tworzydło, and C. Beenakker, Europhys. Lett. **79**, 57003 (2007).
[21] C. W. J. Beenakker and H. van Houten, Solid State Phys. **44**, 1 (1991).
[22] M. I. Katsnelson, K. S. Novoselov, and A. K. Geim, Nat. Phys. **2**, 620 (2006).
[23] M. Katsnelson, Eur. Phys. J. B **52**, 151 (2006).